

Examination of the thermal accommodation coefficient used in the sizing of iron nanoparticles by time-resolved laser-induced incandescence

T. A. Sipkens · N. R. Singh · K. J. Daun · N. Bizmark · M. Ioannidis

Received: 14 November 2014 / Accepted: 20 January 2015 / Published online: 10 February 2015
© Springer-Verlag Berlin Heidelberg 2015

Abstract While time-resolved laser-induced incandescence (TiRe-LII) shows promise as a diagnostic for sizing aerosolized iron nanoparticles, the spectroscopic and heat transfer models needed to interpret TiRe-LII measurements on iron nanoparticles remain uncertain. This paper focuses on three key aspects of the models: the thermal accommodation coefficient; the spectral absorption efficiency; and the evaporation sub-model. Based on a detailed literature review, spectroscopic and heat transfer models are defined and applied to analyze TiRe-LII measurements carried out on iron nanoparticles formed in water and then aerosolized into monatomic and polyatomic carrier gases. A comparative analysis of the results shows nanoparticle sizes that are consistent between carrier gases and thermal accommodation coefficients that follow the expected trends with bath gas molecular mass and structure.

1 Introduction

Over the past decade, researchers have endeavored to extend the capabilities of time-resolved laser-induced incandescence (TiRe-LII), conceived as a diagnostic for sizing soot primary particles [1–4], into a technique for characterizing synthetic nanoaerosols. TiRe-LII uses a laser pulse to heat the nanoparticles within an aerosol sample

to incandescent temperatures, and the spectral incandescence from the energized nanoparticles is then measured as they equilibrate with the ambient gas. Since larger nanoparticles cool more slowly than smaller nanoparticles, the nanoparticle size distribution can, in principle, be inferred by regressing simulated incandescence curves (or, more often, a pyrometric temperature derived from spectral incandescence measurements at multiple wavelengths) to corresponding experimental data. Simulated LII data are generated using a model of the heat transfer between the nanoparticles and surrounding gas. Vander Wal et al. [5] made the first TiRe-LII measurements on synthetic nanoparticles, specifically tungsten, iron, molybdenum, and titanium. While they did not infer nanoparticle sizes from the TiRe-LII data, the incandescence decay suggested that this would be possible provided that nanoparticle cooling could be modeled accurately. TiRe-LII has been subsequently applied to a number of synthetic nanoparticles, including Ag [6], Fe [7–11], Mo [12, 13], Ni [14], MgO [15], TiO₂ [16, 17], Fe₂O₃ [18], SiO₂ [19], and Si [20].

Nanoparticle sizing has been carried out in only a handful of these studies, however, largely because several parameters in the spectroscopic and heat transfer models needed to interpret the TiRe-LII data are unknown. Perhaps most elusive is the thermal accommodation coefficient, α , which specifies the average energy transfer when a gas molecule scatters from the laser-energized nanoparticle. Some researchers have inferred this parameter by comparing TiRe-LII data with nanoparticle sizes determined from ex situ analysis. Starke et al. [7] studied iron nanoparticles formed in a shockwave reactor containing argon and found $\alpha = 0.33$ by matching transmission electron microscopy (TEM) and TiRe-LII-inferred nanoparticle sizes. Eremin et al. [9] also sized iron nanoparticles formed by the condensation of supersaturated iron atom vapor. They, like

T. A. Sipkens · N. R. Singh · K. J. Daun (✉)
Department of Mechanical and Mechatronics Engineering,
University of Waterloo, 200 University Ave. W., Waterloo, ON
N2L 3G1, Canada
e-mail: kjdaun@uwaterloo.ca

N. Bizmark · M. Ioannidis
Department of Chemical Engineering, University of Waterloo,
200 University Ave. W., Waterloo, ON N2L 3G1, Canada

Starke et al. [7], found α by matching TiRe-LII-inferred nanoparticle sizes to those observed in transmission electron micrographs. They reported values of $\alpha = 0.1$ for Fe–Ar, $\alpha = 0.01$ for Fe–He, and $\alpha = 0.2$ for Fe–CO. The TEM analysis also revealed that the iron nanospheres had formed larger fractal-like aggregates, which may suggest that these values underestimate the actual α due to structural shielding of primary particles in the aggregate interior by those on the exterior. Rather than using TEM images, Kock et al. [8] simultaneously inferred α and the geometric mean particle size, $d_{p,g}$, from TEM data, assuming a lognormal distribution for $P(d_p)$ with a geometric standard deviation of $\sigma_g = 1.5$; this analysis is only possible in cases where evaporation plays a significant role in nanoparticle cooling [13]. Kock et al. inferred a value of $\alpha = 0.13$ for Fe–Ar and $\alpha = 0.13$ for Fe–N₂ [8]. The wide variation in reported thermal accommodation coefficients (TACs) for iron nanoparticles implies a fair degree of uncertainty in this parameter.

The absorption efficiency, $E(\mathbf{m}_\lambda)$, used to relate the measured spectral incandescence to the nanoparticle temperatures is also subject to considerable uncertainty. For iron nanoparticles, Kock et al. [8] assumed $E(\mathbf{m}_\lambda)$ to be independent of wavelength in the visible/near infrared spectrum and approximated the $E(\mathbf{m}_\lambda)$ ratio at the measured wavelengths (550 and 694 nm [8]) as unity, a treatment subsequently adopted by Eremin et al. [9–11]. Several experimental (mainly ellipsoidal reflectivity) measurements in the near infrared carried out on molten iron cast doubt on this treatment, however [21–23].

Further uncertainty is introduced through the evaporation sub-model, particularly for smaller nanoparticles, in which case, surface curvature may significantly affect vapor pressure and surface tension. Recent work by Eremin et al. [11] considered surface curvature effects using a combination of the Kelvin equation and changes in surface tension suggested by Nanda et al. [24].

The primary focus of this study is to investigate the radiative properties, thermal accommodation coefficients, and evaporative models needed to interpret TiRe-LII measurements on iron nanoparticles. We first present a thorough review of the radiative properties of molten iron nanoparticles reported in the literature, and a survey of the techniques used to model evaporation from laser-energized iron nanoparticles. Based on these results, spectroscopic and heat transfer models are derived to interpret TiRe-LII measurements carried out on iron nanoparticles in a range of monatomic and polyatomic gases. Unlike previous TiRe-LII experiments on iron nanoparticles, in which the nanoparticles are both synthesized and measured in the gas phase, in this study, the nanoparticles are formed in water and then aerosolized using a pneumatic atomizer. Decoupling the nanoparticle synthesis process from the measurement process provides a means of validation for the

inferred cooling model parameters since TiRe-LII recovered nanoparticle sizes should be identical for each carrier gas. Uncertainties in the inferred parameters are quantified using Bayesian inference. Nanoparticle sizes are found to be similar for all of the gases, but are generally smaller than those inferred through ex situ analysis. The thermal accommodation coefficients follow previously observed trends and are consistent with values derived through molecular dynamics. Similar trends are observed when the ratio of the thermal accommodation coefficient and nanoparticle diameter is inferred solely based on conduction regime cooling.

2 TiRe-LII modeling

Recovering nanoparticle sizes and other parameters from TiRe-LII data requires both a spectroscopic model to relate the observed spectral incandescence to the temperature of the nanoparticles, and a heat transfer model to relate the observed spectral incandescence/effective temperature decay rate to their sizes.

2.1 Spectroscopic model

The spectral incandescence from the laser-heated nanoparticles is given by [13, 20, 25]

$$J_\lambda(t) = C_\lambda \int_0^\infty \frac{\pi d_p^2}{4} \cdot P(d_p) \cdot Q_{\text{abs},\lambda}(d_p) \cdot I_{b,\lambda}[T_p(t, d_p)] \cdot d(d_p) \quad (1)$$

where d_p is the diameter of the nanoparticle, $P(d_p)$ is the particle size distribution, $Q_{\text{abs},\lambda}(d_p)$ is the optical absorption efficiency of the nanoparticles, $I_{b,\lambda}[T_p(t, d_p)]$ is the spectral blackbody radiation at a given temperature, and C_λ is a coefficient defining the detection geometry and spectral efficiency of the collection optics. Nanoparticles having diameters smaller than the wavelength of interest emit and absorb radiation in the Rayleigh regime,

$$Q_{\text{abs},\lambda} = 4\text{Im} \left[\frac{\mathbf{m}_\lambda^2 - 1}{\mathbf{m}_\lambda^2 + 2} \right] x = 4E(\mathbf{m}_\lambda)x \quad (2)$$

where $\mathbf{m}_\lambda = n + ik$ is the complex index of refraction, $E(\mathbf{m}_\lambda)$ is the absorption function, and $x = \pi d_p/\lambda$ is the size parameter.

By measuring the incandescence at two wavelengths, it is possible to use pyrometry to define an effective temperature

$$T_{\text{eff}} = \frac{hc}{k_B} \left(\frac{1}{\lambda_2} - \frac{1}{\lambda_1} \right) \frac{1}{\ln \left[\frac{J_{\lambda_1} \left(\frac{\lambda_1}{\lambda_2} \right) E(\mathbf{m}_{\lambda_2}) C_{\lambda_2}}{J_{\lambda_2} \left(\frac{\lambda_1}{\lambda_2} \right) E(\mathbf{m}_{\lambda_1}) C_{\lambda_1}} \right]} \quad (3)$$

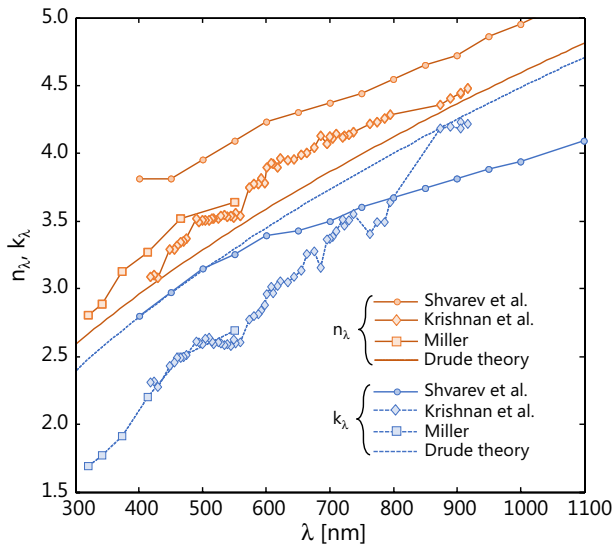


Fig. 1 Real and imaginary refractive indices for molten iron obtained through ellipsometry [21–23] and Drude theory [35]

where $C_{\lambda_2}/C_{\lambda_1}$ is known for the given experimental setup. Equation (3) shows that the effective temperature depends not on $E(\mathbf{m}_\lambda)$ at each detection wavelength, but rather the ratio of these values, $E(\mathbf{m})_r = E(\mathbf{m}_{\lambda_2})/E(\mathbf{m}_{\lambda_1})$.

In contrast to soot, in which $E(\mathbf{m}_\lambda)$ is known to depend on the fuel and local combustion environment (e.g., [26, 27]), for nanoparticles of pure substances, the complex index of refraction of the bulk material should, in principle, provide an accurate assessment of the spectral absorption efficiency provided the nanoparticle diameter is larger than the mean free electron path in the metal [28, 29] and small enough for the Rayleigh approximation to be valid (i.e., $x \ll 1$ [30]). The former condition is clearly satisfied in this experiment, since the mean free electron path in molten iron is approximately 3 nm [31], while the Rayleigh approximation should hold at the laser excitation and detection wavelengths for the nanoparticle sizes expected through this synthesis route [32, 33].

During the TiRe-LII measurement, the iron nanoparticles reach temperatures far exceeding the melting point of iron (1,809 K [34]), so the complex index of refraction for molten iron should be used to calculate $E(\mathbf{m}_\lambda)$. A handful of studies have endeavored to quantify the complex index of refraction, or equivalently the complex dielectric function $\varepsilon = \varepsilon_1 + i\varepsilon_2$, from ellipsometry measurements on molten iron [21–23]; results from these experiments are plotted in Fig. 1. In the case of metals, the spectral variation of ε with wavelength can often be modeled using Drude theory [30],

$$\varepsilon_1(\omega) = n^2 - k^2 = 1 - \frac{\omega_p^2 \tau^2}{1 + \omega^2 \tau^2} \tag{4}$$

and

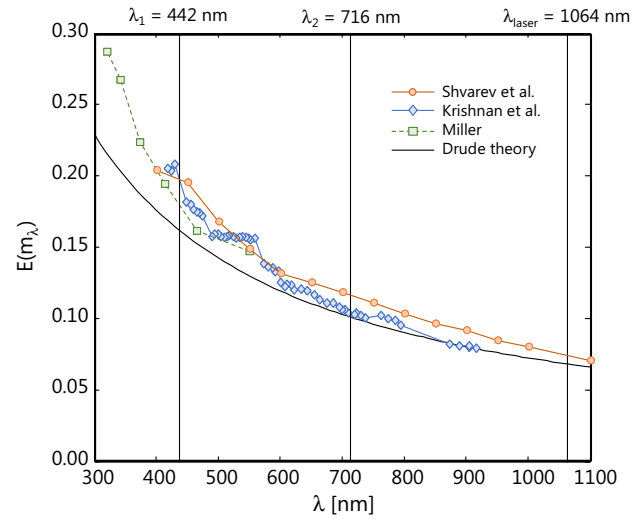


Fig. 2 $E(\mathbf{m}_\lambda)$ of molten iron obtained through ellipsometry [21–23] and Drude theory [35]

$$\varepsilon_2(\omega) = 2nk = \frac{\omega_p^2 \tau}{\omega(1 + \omega^2 \tau^2)} \tag{5}$$

where $\omega = 2\pi\nu = 2\pi c/\lambda$ is the angular frequency, τ is the relaxation time (average time between collisions), ω_p is the plasma frequency, c is the speed of light in a vacuum, and ν is frequency. The plasma frequency is given by

$$\omega_p^2 = \frac{Ne^2}{m\varepsilon_0} \tag{6}$$

where N is the number of free electrons per unit volume, m and e are the mass and charge of an electron, respectively, and ε_0 is the vacuum permittivity. The relaxation time is found from the electrical resistivity of iron,

$$\tau = \frac{m}{\rho_{el}Ne^2} \tag{7}$$

Following these calculations, Kobatake et al. [35] obtained $\omega_p = 6.78 \times 10^{17}$ rad/s and $\tau = 1.69 \times 10^{-19}$ rad/s for molten iron. The real and imaginary complex indices of refraction obtained from Drude theory are plotted in Fig. 1; the trends show good agreement with ellipsometry measurements on molten iron. The corresponding $E(\mathbf{m}_\lambda)$ values are plotted in Fig. 2; vertical lines denote the laser wavelength at 1,064 nm and the two detection wavelengths used in this experiment, 442 and 716 nm. While all previous LII studies of iron nanoparticles have assumed that $E(\mathbf{m})_r = 1$ to infer pyrometric temperatures from incandescence data [8, 10, 11], Fig. 2 shows that both Drude theory and ellipsometry measurements on molten iron [21–23] suggest that $E(\mathbf{m}_\lambda)$ decreases with wavelength. This study will adopt the

$E(\mathbf{m}_\lambda)$ values evaluated from Drude theory, $E(\mathbf{m})_r = E(\mathbf{m}_\lambda = 716 \text{ nm})/E(\mathbf{m}_\lambda = 442 \text{ nm}) \approx 0.63$.

The radiative properties used in the spectroscopic model can be validated by modeling the absorption of laser energy, albeit in a somewhat circular procedure. Following Eremin et al. [10], the complex index of refraction of the nanoparticles at the excitation laser frequency can be inferred from the peak pyrometrically defined temperature found using $E(\mathbf{m})_r$ by performing an energy balance between the start of the laser pulse, when the nanoparticles are at T_g , and the pyrometrically defined peak nanoparticle temperature, $T_{p,\max}$

$$q_{\text{in}} = \rho \frac{\pi d_p^3}{6} [H^\circ(T_{p,\max}) - H^\circ(T_g)] = q_{\text{abs}} - q_{\text{cond}} - q_{\text{evap}} \quad (8)$$

where $H^\circ(T_g)$ and $H^\circ(T_{p,\max})$ are the enthalpy of iron at T_g and $T_{p,\max}$ [34]. While in reality, $T_{p,\max}$ is due to a balance between q_{abs} , q_{evap} , q_{cond} , and the change in enthalpy of the nanoparticles, Eq. (8) can be simplified by neglecting evaporation and conduction heat transfer, in which case

$$\begin{aligned} q_{\text{abs}} &= C_{\text{abs},\lambda_{\text{laser}}} F_0 = \frac{\pi d_p^2}{4} Q_{\text{abs},\lambda_{\text{laser}}}(\mathbf{m}_{\lambda_{\text{laser}}}) F_0 \\ &= \frac{\pi^2 d_p^3}{\lambda_{\text{laser}}} E(\mathbf{m}_{\lambda_{\text{laser}}}) F_0 \end{aligned} \quad (9)$$

where F_0 is the laser fluence in units of J/cm^2 . Substituting Eq. (9) into Eq. (8) gives an expression for $E(\mathbf{m}_{\lambda_{\text{laser}}})$,

$$E(\mathbf{m}_{\lambda_{\text{laser}}}) = \frac{\lambda_{\text{laser}} \rho (T_g) [H^\circ(T_{p,\max}) - H^\circ(T_g)]}{6\pi F_0} \quad (10)$$

with the understanding that the simplifications to Eq. (8) will provide a lower bound estimate for $E(\mathbf{m}_{\lambda_{\text{laser}}})$.

2.2 Nanoparticle cooling model

Interpreting TiRe-LII data also requires a heat transfer model of the nanoparticle cooling rate, which is derived from

$$\rho c_p \frac{\pi d_p^3}{6} \frac{dT_p}{dt} = q_{\text{abs}} - q_{\text{cond}} - q_{\text{evap}} - q_{\text{rad}} \quad (11)$$

where ρ is the density, c_p is the specific heat, q_{abs} is the absorbed laser radiation, q_{cond} is heat transfer by conduction, q_{evap} is heat transfer by evaporation, and q_{rad} is heat transfer due to radiation. While radiation is the means by which the TiRe-LII signal is generated, at atmospheric pressures and nanoparticle diameters expected in this experiment, radiation heat transfer is several orders of magnitude lower than conduction and evaporation and consequently can be neglected in the heat transfer model [36].

2.2.1 Conduction and the thermal accommodation coefficient

The mean free molecular path of the gases considered in this experiment ranges from ~ 40 nm for CO_2 and N_2O to ~ 180 nm for He based on viscosity, which is greater than or equal to the expected nanoparticle sizes; under these conditions, heat conduction occurs in the free molecular regime [37]. In this scenario, gas molecules travel ballistically between the equilibrium gas and the nanoparticle surface without undergoing intermolecular collisions near the nanoparticle. The free molecular conduction heat transfer rate is given by

$$q_{\text{cond}}(t, d_p) = \pi d_p^2 N_g'' \langle E_o - E_i \rangle = \pi d_p^2 \frac{n_g c_{g,t}}{4} \langle E_o - E_i \rangle \quad (12)$$

where N_g'' is the incident gas number flux, $n_g = p_g/(k_B T_g)$ is the molecular number density of the ambient gas, $c_{g,t} = [8k_B T_g/(\pi m_g)]^{1/2}$ is the mean thermal speed of the gas, and $\langle E_o - E_i \rangle$ is the average energy transfer per collision. This last term can be rewritten using the thermal accommodation coefficient, which defines the average energy transfer relative to the maximum allowed by the Second Law of Thermodynamics,

$$\langle E_o - E_i \rangle = \alpha \langle E_o - E_i \rangle_{\text{max}} = \alpha \left(\frac{k_B}{2} \right) \left(2 + \frac{\zeta_{\text{rot}}}{2} \right) (T_p - T_g) \quad (13)$$

where ζ_{rot} is the number of internal (rotational) degrees of freedom in the gas, k_B is Boltzmann's constant, and T_g is the gas temperature. The vibrational energy modes of the gas are likely inaccessible due to the direct nature of gas/surface scattering in TiRe-LII [38]. Monatomic gases have no rotational degrees of freedom, while $\zeta_{\text{rot}} = 2$ for the linear polyatomic molecules (N_2 , CO , NO_2 , and CO_2). The conduction heat transfer rate can now be rewritten as

$$q_{\text{cond}}(t, d_p) = \alpha \pi d_p^2 \frac{p_g c_{g,t}}{8T_g} \left(2 + \frac{\zeta_{\text{rot}}}{2} \right) (T_p - T_g) \quad (14)$$

Trends in the TAC for TiRe-LII measurements have been examined in a number of experimental studies on soot [39] and iron [8, 9], and molecular dynamics (MD) studies on graphite [38, 40], nickel [41], molybdenum [36], iron [36], and silicon [20]. Figure 3 shows these values plotted against the gas molecule to surface atom mass ratio, $\mu = m_g/m_s$. The TAC for monatomic gases generally increases monotonically with increasing mass ratio. This trend does not in itself imply that the mass ratio alone is the key factor in determining the TAC, however, as the potential well depth also increases with the gas molecular mass (number of electrons) for interactions dominated by dispersion-type

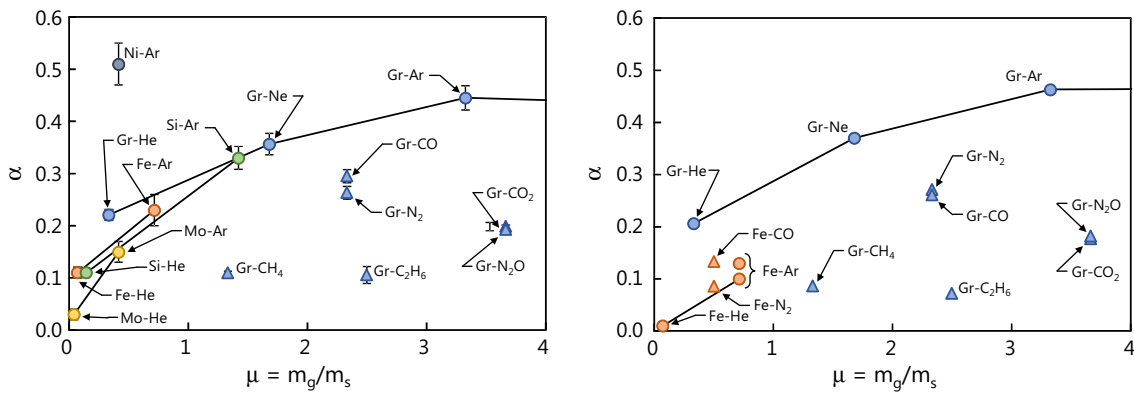


Fig. 3 Thermal accommodation coefficients from MD [36, 38, 40, 41] (left) and TiRe-LII experiments [8, 9, 39] (right) with increasing mass ratio. Solid lines correspond to trends observed in the monoatomic gases in a single study. Error bounds of MD values correspond

to the stochastic variation and do not account for errors that may result from inaccuracy in the underlying physics. Circles correspond to monoatomic gases and triangles correspond to polyatomic gases

forces. Indeed, a notable exception to the trend of α versus μ is the MD-derived TAC for nickel nanoparticles in argon; the gas/surface interaction for this system is dominated by a Casimir-Polder interaction, giving rise to a much deeper potential well than what would occur for a system of similar μ dominated by dispersion forces [41]. Figure 3 also shows that the TAC for polyatomic gases lies below those of monoatomic gases having similar μ , which indicates that surface energy transfers preferentially to the translational modes of the gas molecule over the rotational modes.

2.2.2 Evaporation and the vapor properties

Heat transfer due to evaporation also occurs in the free molecular regime,

$$q_{\text{evap}}(t, d_p) = \Delta H_v \pi d_p^2 N_v'' = \Delta H_v \pi d_p^2 \frac{n_v c_v}{4} \quad (15)$$

where ΔH_v is the heat of vaporization of iron atoms, N_v'' is the iron vapor number flux, $n_v = p_v / (k_B T_p)$ is the vapor number density, and $c_v = [8k_B T_p / (\pi m_p)]^{1/2}$ is the mean thermal speed of the vapor. This analysis presumes that individual iron atoms evaporate instead of iron nanoclusters, following Refs. [8–11], and that recondensation of evaporated species is negligible, which is reasonable given the large surface energy of the laser-energized nanoparticles relative to the potential well depth. There are a number of ways to calculate the heat of vaporization; in this study, ΔH_v is found using Watson’s equation [42],

$$\Delta H_v = K \left(1 - \frac{T_p}{T_{\text{cr}}} \right)^{0.38} \quad (16)$$

where K is a material constant and T_{cr} is the critical temperature of iron [43]. Assuming that the nanoparticle surface

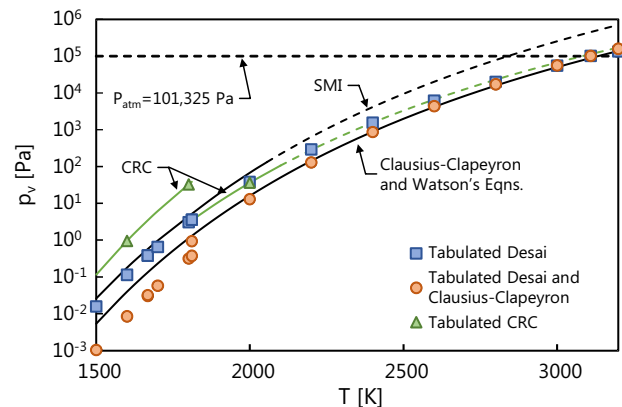


Fig. 4 Vapor pressure of iron as a function of nanoparticle temperature [44–46]. Solid lines correspond to continuous equations evaluated across the temperature range. Dashed lines, except for the line marking atmospheric pressure, are extrapolations of equations beyond the recommended temperatures. Points correspond to tabulated values

and vapor phases are in quasi-equilibrium, the heat of vaporization and vapor pressure may then be related using the Clausius–Clapeyron equation

$$\ln(p_{v,o}) = -\frac{\Delta H_v}{R} \frac{1}{T_p} + C \quad (17)$$

where R is the universal gas constant and C is a material constant. On the other hand, Kock et al. [8] and Eremin et al. [9–11] adopted the vapor pressure of the bulk materials reported in the CRC handbook [44] and then used Eq. (17) to evaluate the heat of vaporization. Given the large temperature variation of laser-energized nanoparticles during cooling, it is insightful to examine the variation of the vapor pressure with temperature as calculated through a variety of alternative techniques. Figure 4 compares p_v

obtained from Ref. [44] with those obtained from combining Watson's equation and the Clausius–Clapeyron equation (used in the present work with the reference state point corresponding to the boiling temperature given in Ref. [44]), and several other sources [45, 46]. All these methods produce very similar vapor pressures over the temperature range typical of cooling nanoparticles.

Surface curvature may also influence evaporative cooling, since a small radius of curvature increases the surface energy [11, 20, 47]. The Kelvin equation modifies the vapor pressure predicted for a flat surface, $p_{v,o}$, according to

$$p_v = p_{v,o} \exp \left[\frac{4\gamma_s}{d_p \rho R_s T_p} \right] \quad (18)$$

where γ_s is the surface tension of the nanoparticle material, taken in this case as a function of temperature from Keene [48], and R_s is the specific gas constant. It has been further speculated that nanoparticle surface tension may also deviate from its bulk value. Historically, the Tolman equation [49]

$$\gamma_s = \frac{\gamma_{s,o}}{1 + 4\delta/d_p} \quad (19)$$

has been used to calculate deviations in the surface tension from its bulk value. In this equation, $\gamma_{s,o}$ is the surface tension of the bulk material and δ is the Tolman length, originally taken as the atomic diameter, h , of the substrate material. There is, however, a great deal of controversy over the correct value of the Tolman length, and even the underlying applicability of the Tolman equation. Kuhlmann et al. [47] and Eremin et al. [11], for example, cite Nanda et al. [24], who express skepticism in the applicability of the Tolman equation at very small nanoparticle diameters and in the value of the Tolman length over a wider range of nanoparticle sizes. As the Tolman equation is considered valid at larger nanoparticle sizes (generally $d_p > 50 \cdot \sigma_{LJ}$ [50], corresponding to approximately $d_p > 7$ nm for iron), most studies, at least initially, evaluate the Tolman length in the limit $d_p \rightarrow \infty$, that is, δ_∞ . Koga et al. [50] consider two candidates for δ_∞ , the more extreme of which gives $\delta_\infty = -0.23 \cdot \sigma_{LJ}$, where σ_{LJ} is the Lennard-Jones 6–12 equilibrium distance (0.2517 nm in the parameterization of iron by Mohri et al. [51]). This choice of δ_∞ corresponds to an increase in surface tension with decreasing nanoparticle diameter and acts as a basis for assessing other δ candidates. To investigate the validity of the Tolman equation, Koga et al. [50] carried out MD simulations on a Lennard-Jones liquid and found an inflection in the surface tension at $d_p = 10 \cdot \sigma_{LJ}$; further reduction of d_p corresponds to a drop in surface tension, contrary to what is predicted by the Tolman equation with $\delta_\infty = -0.23 \cdot \sigma_{LJ}$. Lei et al. [52] propose a maximum value of $\delta_\infty = 0.11 \cdot \sigma_{LJ}$, while Lu and Jiang [53] suggest $\delta_\infty = h$.

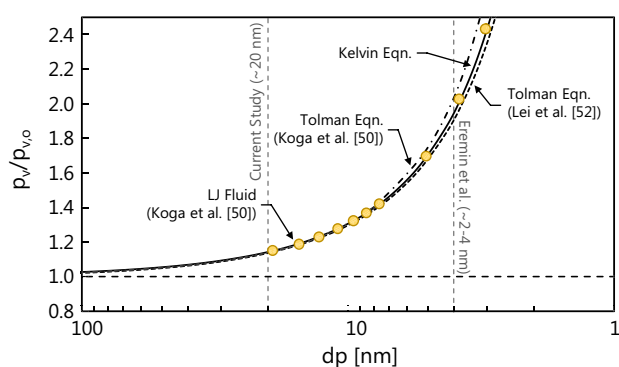


Fig. 5 Reduced vapor pressure of iron as a function of nanoparticle size. The *solid line* corresponds to the vapor pressure using the Kelvin equation with the surface tension of the bulk material. *Dashed lines* correspond to the Kelvin equation with a surface tension corrected using the Tolman equation with $\delta = -0.23 \cdot \sigma_{LJ}$ [50] and $\delta = 0.11 \cdot \sigma_{LJ}$ [52]. Points correspond to Lennard-Jones simulations [50]. *Vertical dashed lines* correspond to approximate nanoparticle sizes in the current study and Eremin et al. [9]

It should be noted that this is a very active area of research and there remains considerable uncertainty in the choice of Tolman length and the underlying validity of Tolman's equation [54, 55]. To determine how this uncertainty impacts TiRe-LII measurements, the vapor pressure is plotted in Fig. 5 for various choices of the Tolman length, alongside the vapor pressure evaluated using the bulk surface tension in the Kelvin equation. Figure 5 shows that this effect has a negligible influence on surface tension at nanoparticle sizes above 5 nm, where the models all lie within ten percent of each other. At nanoparticle sizes below this threshold, variation in vapor pressure is discernable only at the extreme endpoints of the range $[-0.23 \sigma_{LJ}, h]$ proposed in the literature. For the sake of the current work, in which nanoparticle sizes are always greater than 5 nm, evaporation from the nanoparticles can be modeled with sufficient accuracy using the Kelvin equation alone. Presumably, similar principles can be applied to other materials used in TiRe-LII, by scaling the effects of the Tolman equation based on σ_{LJ} .

3 Experimental procedure

The spectroscopic and heat transfer models defined above are applied to TiRe-LII measurements carried out on iron nanoparticles formed in aqueous solution and then aerosolized using a TSI Model 3076 pneumatic atomizer operating in recirculation mode. The experimental method is summarized in Fig. 6. Zero-valent iron nanoparticles are synthesized by reducing ferrous iron (Fe^{2+}) with a solution of sodium borohydride (NaBH_4), using the procedure described in Refs. [32, 33]. For a final volume of

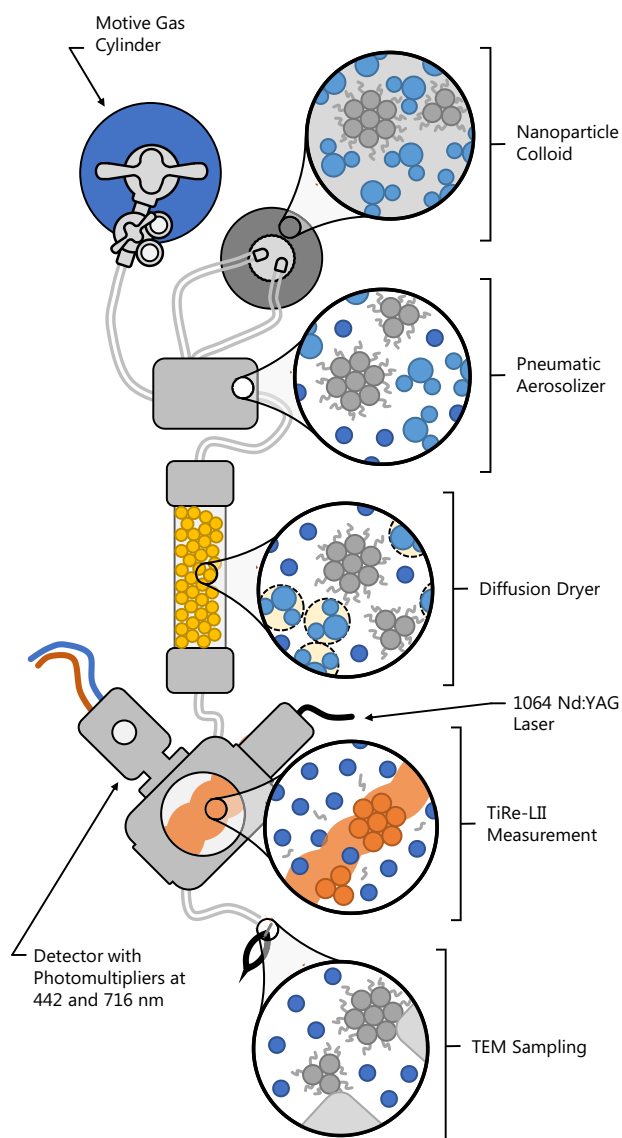
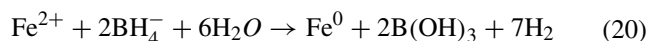


Fig. 6 The iron nanocolloid is induced into a pneumatic atomizer by the motive gas and leaves as $0.3\ \mu\text{m}$ droplets. The droplets then pass through a diffusion dryer with a desiccant to remove water, leaving a dry aerosol of iron nanoparticles. The nanoparticles flow into the TiRe-LII measurement chamber where a sample is heated using a 1,064 Nd:YAG laser. The resultant incandescence is measured at 442 and 716 nm. TEM grids are collected at the system exhaust

100 mL, 1:2.4 volume ratio of iron (II) sulfate heptahydrate ($\text{FeSO}_4 \cdot 7\text{H}_2\text{O}$) solution (1.28 mol/L) and carboxymethylcellulose (CMC) ($\sim 250\ \text{kDa}$) solution (to a final concentration of 0.85 wt%), all in ultrapure deionized water, are combined in a flask. This dilution ensures that each atomized droplet (approximately $0.3\ \mu\text{m}$ in diameter as specified in the pneumatic atomizer manual) contains, on average, one iron nanoparticle. Adding the CMC stabilizer to the iron salt solution under vigorous agitation for $\sim 20\ \text{min}$ ensures formation of the CMC- Fe^{2+} complex,

which should prevent the iron nanoparticles from agglomerating. Addition of 15 mL sodium borohydride solution (4.26 mol/L) under continuous vigorous stirring results in a black colloidal suspension of CMC-stabilized zero-valent iron nanoparticles according to



Motive gas (He, Ne, Ar, CO, N_2 , CO_2 , or N_2O) supplied at a regulator pressure of 200 kPa (30 psi) flows through an orifice into a low-pressure mixing chamber; the nanoparticle solution is drawn up a vertical channel into the mixing chamber, where it is atomized by the gas stream. The droplet-laden gas then impacts a wall; large droplets condense and flow back into the solution container, while small droplets exit in the aerosol stream. The water droplets then flow through a diffusion dryer filled with a silica gel desiccant, which removes the water and leaves the CMC-coated iron nanoparticles in the aerosol.

The dry aerosol then enters the measurement chamber of an Artium 200 M TiRe-LII system. The pressure of the gas entering the measurement chamber was monitored using a pressure transducer and was shown to be within $\pm 5\ \text{kPa}$ of atmospheric pressure (101.3 kPa). A 1,064 nm Nd:YAG laser pulse, having an approximately top-hat fluence profile, energizes the nanoparticles within a $23\ \text{mm} \times 23\ \text{mm}$ probe volume. The incandescence of these nanoparticles is imaged onto two photomultiplier tubes, which measure the time-resolved incandescence at 442 and 716 nm every 2 ns. Incandescence signals were collected from 250 pulses for each aerosol type. Uncertainties are estimated using Bayesian inference, as described in the “Appendix.” Throughout each testing run, LII measurements were carried out on iron nanoparticles in argon between measurements on other aerosol types to ensure that the test conditions remained unchanged throughout the experiment.

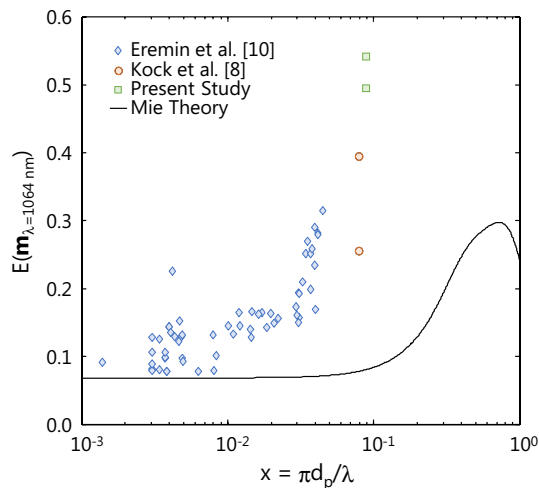
4 Experimental results

4.1 Laser absorption analysis

The $E(\mathbf{m}_{\lambda, \text{laser}})$ values recovered for CMC-capped and uncapped iron nanoparticles in argon are shown in Table 1. The peak pyrometric temperature measured from uncapped iron nanoparticles slightly exceeds the boiling point of iron (3,133 K [34]); this may suggest that the molten iron nanoparticles are superheated or may be due to uncertainty in $E(\mathbf{m})_r$. Accordingly, the increase in nanoparticle enthalpy is approximated by $c_p (T_{p, \text{max}} - T_g)$, where $c_p = 824\ \text{J}/(\text{kg K})$ is the specific heat of molten iron near its boiling point [34].

Table 1 $E(\mathbf{m}_{\lambda_{\text{laser}}})$ values from Kock et al. [8] and the present study (for Fe–Ar) calculated using Eq. (10)

| Gas-surface pair | F_0 (J/cm ²) | $T_{p,0}$ (K) | $E(\mathbf{m}_{\lambda_{\text{laser}}})$ |
|----------------------------|----------------------------|---------------|--|
| Present study (CMC capped) | 0.22 | 3,025 | 0.50 |
| Present study (Uncapped) | 0.22 | 3,277 | 0.54 |
| Kock et al. [8] | 0.32 | 2,476 | 0.26 |
| Kock et al. [8] | 0.19 | 2,285 | 0.39 |

**Fig. 7** Plot of $E(\mathbf{m}_{\lambda_{\text{laser}}})$ calculated using Eq. (10) from Kock et al. [8], Eremin et al. [9], and the present study versus the size parameter, $x = \pi d_p/\lambda$. The solid curve shows results calculated using Mie theory with $\mathbf{m}_\lambda = n_\lambda + ik_\lambda$ obtained from Drude theory

The recovered $E(\mathbf{m}_{\lambda_{\text{laser}}})$ values are considerably higher than either Drude theory or any of the experimental ellipsometry data would suggest. While Kock et al. [8] do not explicitly calculate $E(\mathbf{m}_{\lambda_{\text{laser}}})$ in their paper, a reanalysis of the peak temperatures reported at two fluences shows $E(\mathbf{m}_{\lambda_{\text{laser}}})$ values similar to those found in this study. Eremin et al. [10] carried out TiRe-LII on iron nanoparticles ranging between 1 and 16 nm and, through a similar technique, found that the inferred $E(\mathbf{m}_{\lambda_{\text{laser}}})$ varied with nanoparticle size; the smallest nanoparticles correspond to values similar to Drude theory predictions and increase with d_p to a value of approximately 0.3. These results are plotted versus $x = \pi d_p/\lambda_{\text{laser}}$ in Fig. 7. Figure 7 also shows an “effective” $E(\mathbf{m}_{\lambda_{\text{laser}}})$ derived by calculating the absorption cross section using Mie theory [30] with the complex refractive index found using Drude theory (Fig. 1) and dividing by $4x$.

Eremin et al. [10] hypothesize that the deviation of $E(\mathbf{m}_{\lambda_{\text{laser}}})$ from the value predicted using the complex refractive index of the bulk material could be due to the small size of the nanoparticles. As noted in Sect. 2.1, however, the absorption cross section should become size

dependent only when the nanoparticle diameter approaches the mean free electron path (i.e., when electron confinement becomes important), which, as noted above, is much smaller than the nanoparticle sizes investigated here. This is also borne out by non-LII experiments, which have verified that the spectral absorption cross section of similar-sized nanoparticles can be accurately predicted using the complex index of refraction of the bulk material (e.g., [56]). Figure 1 also discounts the possibility that the unexpectedly large $E(\mathbf{m}_{\lambda_{\text{laser}}})$ values could be due to an excursion outside of the Rayleigh regime since: (a) this effect is not large enough to account for the $E(\mathbf{m}_{\lambda_{\text{laser}}})$ values inferred through Eq. (10) and (b) the Rayleigh regime assumption is valid for $x < 0.1$, which, for $\lambda_{\text{laser}} = 1,064$ nm, corresponds to nanoparticles larger than 100 nm. An alternative hypothesis is that non-incandescence laser-induced emission (LIE) could be contaminating the prompt LII signal. In their pioneering LII measurements on iron nanoparticles, Vander Wal et al. [5] identified short-lived, non-incandescent LIE in spectrally resolved LII measurements on iron nanoparticles that can be distinguished from incandescence by their narrow spectral features, although these measurements were made using higher fluences ($F_0 \geq 1.2$ J/cm²) than those employed in this study and occurred at wavelengths shorter than 400 nm. Maffi et al. [16] observed similar phenomenon in their measurements on titania. In a later work, however, Vander Wal et al. [57] suggest that laser-induced microplasmas can give rise to pseudo-blackbody spectra, so, at short timescales after the laser pulse, the LII signal may be dominated by blackbody emission from a plasma of sublimed iron ions, and not incandescence from the nanoparticle. This plasma can also absorb laser irradiation with a much greater efficiency than the nanoparticle, which could account for the discrepancy between the $E(\mathbf{m}_{\lambda_{\text{laser}}})$ predicted using Drude theory, and the value inferred from an energy balance. This hypothesis could also explain the trends of $E(\mathbf{m}_{\lambda_{\text{laser}}})$ versus nanoparticle size shown in Fig. 7, since it is possible that the smaller nanoparticles are not producing a significant plasma due to their elevated surface energy. This hypothesis requires further experimental and theoretical study to confirm if it is indeed the case.

4.2 Analysis of evaporation and conduction regime data

We next attempt to recover the thermal accommodation coefficient and nanoparticle size by regressing modeled effective temperatures to experimentally determined quantities. As noted above, the TiRe-LII data are interpreted using the $E(\mathbf{m})_r$ value obtained from Drude theory and by assuming that the nanoparticle sizes are monodisperse. Sample experimental signals are included in Fig. 8 along with the corresponding best fits given the monodisperse assumption. The Fe–Ar curve is also accompanied with

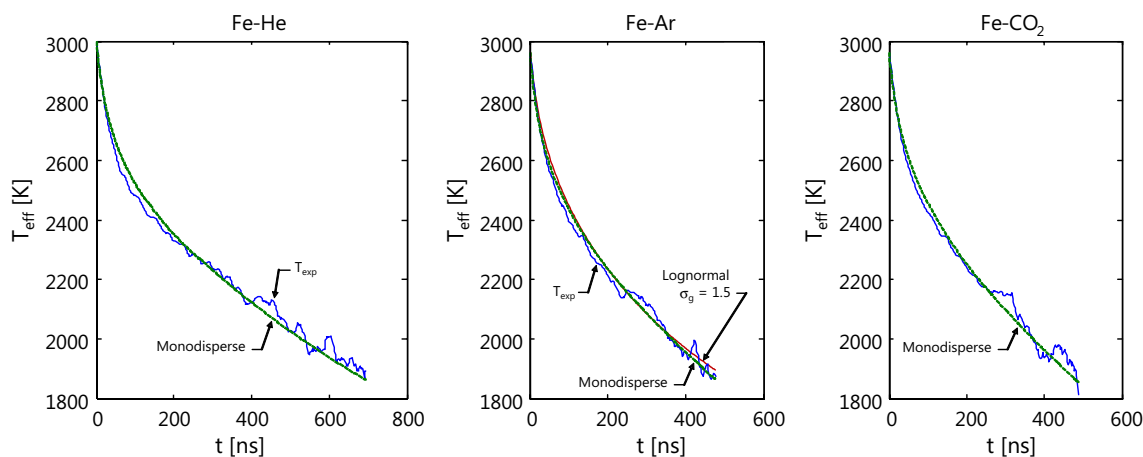


Fig. 8 Experimental effective temperature decay for Fe–He, Fe–Ar, and Fe–CO. Curves are plotted with their accompanying best fits. While modeled data generated using a monodisperse distribution fit

the experimental data over the entire measurement duration, modeled data generated using a lognormal distribution with $\sigma_g = 1.5$ deviate from the experimental data at longer cooling times

a polydisperse fit assuming a lognormal nanoparticle size distribution with a distribution width corresponding to $\sigma_g = 1.5$, which is more typical for nanoparticles formed in the gas phase (e.g., [8–11, 20]). Treating the nanoparticle size distribution in this manner creates fits with minor observable differences. The differences that are observed are a result of too much curvature, with the existence of larger nanoparticles causing larger effective temperatures at later cooling times. Given the significant increased computation effort and reductions in goodness of fit, the monodisperse assumption was taken as appropriate for the current work. Any small increases in the distribution width away from the monodisperse assumption will result in increases in both the TAC and nanoparticle size, with the TAC increasing faster with increasing distribution width.

The results of this inference are summarized in Fig. 9 and Table 2. Error bounds are evaluated at 14 % of their nominal value based on 75,000 Markov chain Monte Carlo (MCMC) samples calculated for iron nanoparticles in argon.

Trends in the thermal accommodation coefficients follow those reported by Daun et al. [38], with TACs for monatomic gases increasing monotonically with μ and the values for the polyatomic gases lying below this observed trend. The TACs of monatomic gases are generally larger than those reported in previous experimental TiRe-LII studies on iron nanoparticles [8, 9], but they are close to values for Fe–He and Fe–Ar found from molecular dynamics [36]. In contrast to previous studies [8, 9], which calculated α assuming that all surface energy is accommodated into the translational mode of the gas molecule (i.e., $\langle E_o - E_i \rangle_{\max} = 2k_B(T_s - T_g)$), the TACs for

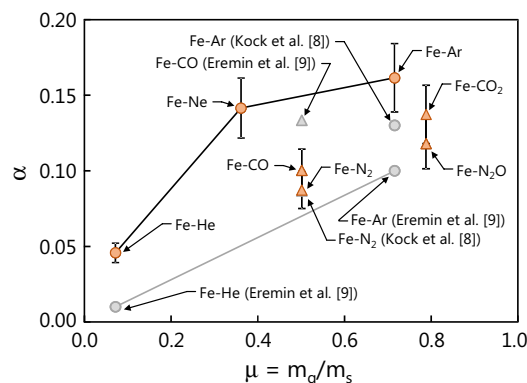


Fig. 9 Thermal accommodation coefficients inferred using the full (evaporation + conduction) cooling model. Error bounds correspond to 14 % of the nominal value based on one standard deviation of the mean of 75,000 MCMC samples

Table 2 The results of an evaporation regime inference of α and d_p with error bounds corresponding to 14 % of the nominal value based on one standard deviation of 75,000 MCMC samples

| Gas-surface pair | $\mu = m_g/m_s$ | α | α (Prev. studies) | α (MD study) | d_p (nm) |
|---------------------|-----------------|-----------------|--------------------------|---------------------|------------|
| Fe–He | 0.07 | 0.05 ± 0.01 | 0.01 [9] | 0.11 [36] | 20 ± 2 |
| Fe–Ne | 0.36 | 1.14 ± 0.02 | – | – | 18 ± 3 |
| Fe–N ₂ | 0.50 | 0.09 ± 0.01 | 0.09 [8] | – | 18 ± 3 |
| Fe–CO | 0.50 | 0.10 ± 0.01 | 0.13 [9] | – | 18 ± 3 |
| Fe–Ar | 0.72 | 0.16 ± 0.02 | 0.013 [8], 0.1 [9] | 0.23 [36] | 15 ± 2 |
| Fe–N ₂ O | 0.79 | 0.12 ± 0.02 | – | – | 18 ± 3 |
| Fe–CO ₂ | 0.79 | 0.14 ± 0.02 | – | – | 17 ± 2 |

Table 3 Variation in the inferred TAC and nanoparticle size with $E(\mathbf{m})_r$. $E(\mathbf{m})_r = 1$ corresponds to the assumption adopted in literature by Kock et al. [8] and Eremin et al. [9–11]

| Gas-surface pair | Drude theory $E(\mathbf{m})_r = 0.63$ | | Krishnan et al. [21] $E(\mathbf{m})_r = 0.54$ | | Shvarev et al. [23] $E(\mathbf{m})_r = 0.59$ | | $E(\mathbf{m})_r = 1$ | |
|---------------------|--|----------|--|----------|---|----------|-----------------------|----------|
| | d_p (nm) | α | d_p (nm) | α | d_p (nm) | α | d_p (nm) | α |
| Fe–He | 20 | 0.05 | 15 | 0.04 | 18 | 0.04 | 76 | 0.19 |
| Fe–Ne | 18 | 0.14 | 13 | 0.10 | 16 | 0.12 | 70 | 0.59 |
| Fe–N ₂ | 18 | 0.09 | 14 | 0.07 | 15 | 0.07 | 63 | 0.32 |
| Fe–CO | 20 | 0.10 | 17 | 0.10 | 22 | 0.13 | 83 | 0.49 |
| Fe–Ar | 15 | 0.16 | 10 | 0.11 | 13 | 0.14 | 56 | 0.64 |
| Fe–N ₂ O | 18 | 0.12 | 13 | 0.08 | 16 | 0.10 | 68 | 0.47 |
| Fe–CO ₂ | 18 | 0.14 | 12 | 0.10 | 15 | 0.12 | 56 | 0.44 |
| Ave. d_p | 18 | – | 13 | – | 16 | – | 67 | – |

the polyatomic gases in the present study were defined according to Eq. (13). Accordingly, TACs reported in Refs. [8] and [9] are multiplied by 2/3, allowing for energy transfer into two rotational degrees of freedom. After this adjustment, the values for Fe–N₂ and Fe–CO reported in previous studies [8, 9] are consistent with those found in the present study.

Inferred nanoparticle sizes are consistent across the various gases, and all lie within two standard deviations of the uncertainties found through MCMC (see “Appendix”). This result highlights the benefit of liquid-phase synthesis: even though the observed temperature decay rates vary considerably between the gases, the inferred nanoparticle sizes are similar, as one would expect as they are derived from a common nanocolloid stock solution, and the thermal accommodation coefficients follow expected trends based on molecular mass and structure. The inferred nanoparticle sizes also lie within the range of nanoparticle sizes expected from this synthesis technique, which is reported to be between 15 and 40 nm [32, 33].

As noted in Sect. 2, a key source of uncertainty is the value of $E(\mathbf{m})_r$ used to interpret the spectral incandescence measurements. Table 3 shows how various choices of $E(\mathbf{m})_r$ influence the inferred nanoparticle sizes and TACs; generally, both the TAC and nanoparticle size increase with increasing $E(\mathbf{m})_r$, reaching the highest values when $E(\mathbf{m})_r = 1$. In contrast to previous studies, the nanoparticle sizes and TACs inferred using $E(\mathbf{m})_r < 1$ appear to be more consistent with the expected values compared with assuming $E(\mathbf{m})_r = 1$. A somewhat perplexing outcome, however, is that the TACs inferred assuming $E(\mathbf{m})_r = 0.63$, following Drude theory, are consistent with those reported by Kock et al. [8] and Eremin et al. [9], even though these studies interpreted the TiRe-LII data assuming $E(\mathbf{m})_r = 1$. As noted in Sect. 2.1, however, there appears to be significant experimental and theoretical evidence that $E(\mathbf{m})_r$ is not unity; this inconsistency requires further explanation.

Table 4 Conduction-only inference of α/d_p with error bounds corresponding to 14 % of the nominal value based on one standard deviation of the mean of 75,000 MCMC samples. The final column shows the TAC assuming $d_p = 18$ nm

| Gas-Surface Pair | $\mu = m_g/m_s$ | $\alpha/d_p \times 10^{-2} \text{ (nm}^{-1}\text{)}$ | $\alpha \text{ (} d_p = 18 \text{ nm)}$ |
|---------------------|-----------------|--|---|
| Fe–He | 0.07 | 0.21 ± 0.03 | 0.04 ± 0.01 |
| Fe–Ne | 0.36 | 0.78 ± 0.11 | 0.014 ± 0.02 |
| Fe–N ₂ | 0.50 | 0.46 ± 0.06 | 0.08 ± 0.01 |
| Fe–CO | 0.50 | 0.50 ± 0.07 | 0.09 ± 0.01 |
| Fe–Ar | 0.72 | 1.06 ± 0.15 | 0.19 ± 0.03 |
| Fe–N ₂ O | 0.79 | 0.61 ± 0.08 | 0.11 ± 0.02 |
| Fe–CO ₂ | 0.79 | 0.70 ± 0.10 | 0.13 ± 0.02 |

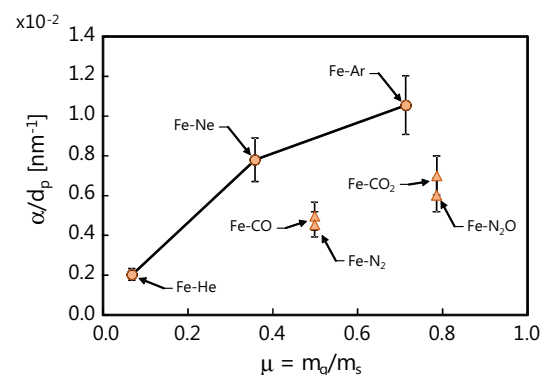


Fig. 10 α/d_p inferred from the data subset corresponding to conduction-dominated cooling ($T_p < 2,400$ K.) Error bounds correspond to 14 % of the nominal value based on one standard deviation of the mean of 75,000 MCMC samples

4.3 Analysis of conduction regime data

As a further verification of these inferences, we also infer parameters using effective temperatures measured during conduction-dominated cooling, corresponding to temperature less than 2,400 K. While excluding evaporated-dominated cooling from the analysis avoids uncertainties

associated with the evaporation model, in conduction-dominated cooling, α and d_p appear as a ratio in Eqs. (11) and (12), which means that it is impossible to infer each of these parameters independently [13, 39]. Since d_p should be the same for each carrier gas, plotting inferred α/d_p values should also reveal how α changes with molecular mass and structure of the carrier gas. (This is equivalent to inspecting the slope of the cooling curve when it is plotted on a semilog scale, following [39].) The results of this inference, summarized in Table 4 and Fig. 10, show TAC trends that match the α values inferred from the full set of cooling data, shown in Fig. 9.

A thermal accommodation coefficient can be obtained from these estimates by using an average nanoparticle diameter inferred from analyzing data from both the evaporation and conduction regimes, which is taken to be $d_p = 18$ nm. The TACs found from this treatment are also given in Table 2 along with those from previous experimental studies [8, 9]. Generally, the TACs obtained using the conduction regime data lay within the reported credible intervals inferred using the complete dataset.

4.4 Ex situ nanoparticle size measurements

Attempts were also made to characterize the nanoparticle size distributions through a variety of ex situ analyses. Initially, nanoparticles were impaction-sampled from the aerosol by holding a 200-mesh copper TEM grid perpendicular to the exhaust stream of the TiRe-LII measurement chamber, but subsequent TEM micrographs showed a very sparse population of large iron nanoparticles (~200–500 nm). This result is not unexpected, since it is notoriously difficult to extract nanoparticles from an ambient aerosol onto a TEM grid, and impaction sampling may result in a distribution biased toward larger nanoparticles. In an attempt to improve sampling efficiency, an electrostatic precipitator (ESPnano, Model 100) was used to sample the exhaust stream for 100 s. TEM micrographs revealed a wider distribution of nanoparticle sizes than previously observed, ranging from approximately 20 nm (Fig. 11a) to 700 nm (Fig. 11b), with the majority of distinguishable iron nanoparticles averaging around 200–300 nm. Additional structural features including the clustering of iron nanoparticles (Fig. 11c) and the CMC coating (Fig. 11d) on some of the nanoparticles can also be seen. Nevertheless, the TEM grids remained too sparse to permit a detailed statistical sampling of the TEM images.

Dynamic light scattering (DLS) measurements were also carried out on stock nanocolloid solutions synthesized following the procedure described above and then diluted 1:1,000 in deionized water. The diluted solutions were then ultrasonically dispersed and analyzed in a Vasco DL 135 instrument using a Padé-Laplace fit model. In this

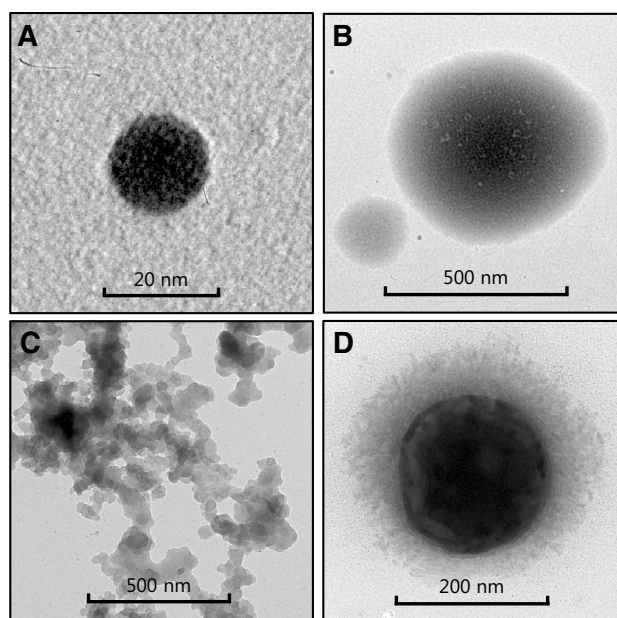


Fig. 11 TEM images showing a variety of iron nanospheres and agglomerates of various sizes from the current set of experiments. The iron nanoparticles are regularly surrounded by CMC

technique, a laser is shone through the diluted nanocolloid sample, and the nanoparticle hydrodynamic diameter is inferred from the autocorrelation of scattered intensity caused by the Brownian motion of the nanoparticles within the fluid. A refractive index of 2.87 was assumed for the CMC-coated iron nanoparticles [58]. The results suggest that the solution contains two types of nanoparticles that both have narrow size distributions: a large population of large nanoparticles ($d_p > 1 \mu\text{m}$), presumably clusters of excess CMC or CMC-coated nanoparticles, and a small population of much smaller nanoparticles, corresponding to isolated CMC-coated iron nanospheres. Two stock solutions were analyzed: The first solution was ultrasonically dispersed for 15 min immediately after synthesis and then measured to reveal a number hydrodynamic diameter of 25 nm, which is consistent with TiRe-LII inferred diameters. The second solution was ultrasonically dispersed for 10 min after synthesis and measured to reveal a nanosphere hydrodynamic diameter of 60 nm. Subsequent measurements 20 and 30 min after synthesis showed diameters of 160 and 156 nm, respectively.

These results appear to suggest that the nanoparticle size can vary significantly between stock nanocolloids, and that the mean nanoparticle hydrodynamic diameter appears to grow as the solution ages. We initially hypothesized that the latter effect was due to oxidization, suggested by the appearance of an orange-red precipitate after approximately 20 min. Assuming the most common form of iron oxidation,



and based on the corresponding molar densities, one would expect an increase in diameter of approximately 200 %. Consequently, oxidation alone does not account for the increase in hydrodynamic diameters observed in the DLS measurements. Instead, we suspect that some physical or chemical reaction within the nanocolloid (possibly involving agglomeration of the CMC-coated nanoparticles, or excess CMC in the solution) is affecting the Brownian motion of the nanoparticles.

5 Conclusions

Time-resolved laser-induced incandescence (TiRe-LII) is a potent tool for characterizing gas-borne iron nanoparticles, but considerable uncertainty remains in the spectroscopic and heat transfer models needed to interpret the TiRe-LII data. This paper focuses on the radiative properties, the evaporation model, and the thermal accommodation coefficient for TiRe-LII measurements of iron nanoparticles. While all previous studies examine iron nanoparticles synthesized in the gas phase, in this work the iron nanoparticles are synthesized in water and then aerosolized into various monatomic and polyatomic motive gases using a pneumatic atomizer.

While previous TiRe-LII studies on iron nanoparticles assume that the spectral absorption function is constant over the measurement wavelengths, ellipsometry measurements on molten iron and Drude theory suggest that the variation of $E(\mathbf{m}_\lambda)$ over the visible and near infrared wavelengths cannot be neglected. An energy balance over the laser pulse heating period also shows that the effective absorption function is considerably larger than what would be predicted from the radiative properties of molten iron, a phenomenon also observed in previous TiRe-LII measurements on iron nanoparticles. While it may be possible that a microplasma surrounding the laser-heated iron nanoparticles could account for these inconsistencies, further experimental and analytical investigation is needed to verify this hypothesis.

A comparative analysis of nanoparticle sizes and thermal accommodation coefficients inferred from the TiRe-LII data reveals similar nanoparticle sizes for each carrier gas and TACs that follow expected trends in the literature. Thermal accommodation coefficients found using the full dataset and the evaporation/conduction cooling model also match the α/d_p values inferred from a subset of the data corresponding to conduction-dominated cooling. Unfortunately, the nanoparticle sizes inferred from ex situ (TEM and DLS) techniques were inconclusive; TEM images

suggested much larger nanoparticles, while DLS measurements showed nanoparticle diameters that varied between stock solutions and grew over time.

The results of this study highlight the benefit of comparing TiRe-LII measurements made by aerosolizing nanoparticles into a variety of carrier gases. We intend to continue this process by investigating other types of gases and extending our study to other nanoparticle materials. Future studies are also planned, which will use a spectrometer and gated ICCD to measure the incandescence over a continuous spectrum; these measurements will greatly help elucidate the radiative properties of the laser-energized iron nanoparticles.

Acknowledgments This research was supported by the National Science and Engineering Research Council of Canada (NSERC), the Canadian Foundation for Innovation-Leaders Opportunity Fund (CFI-LOF), and the Waterloo Institute for Nanotechnology (WIN). Transmission electron microscopy was carried out using the facilities of the Canadian Centre for Electron Microscopy.

Appendix: Uncertainty analysis through Bayesian estimation

TiRe-LII data are analyzed using Bayesian inference. In this technique, a posterior distribution, $P(\mathbf{x}|\mathbf{b})$, of the quantities-of-interest in \mathbf{x} conditional on observed data in \mathbf{b} is found using Bayes' equation

$$P(\mathbf{x}|\mathbf{b}) = \frac{P(\mathbf{b}|\mathbf{x})P_{\text{pr}}(\mathbf{x})}{P(\mathbf{b})} \quad (22)$$

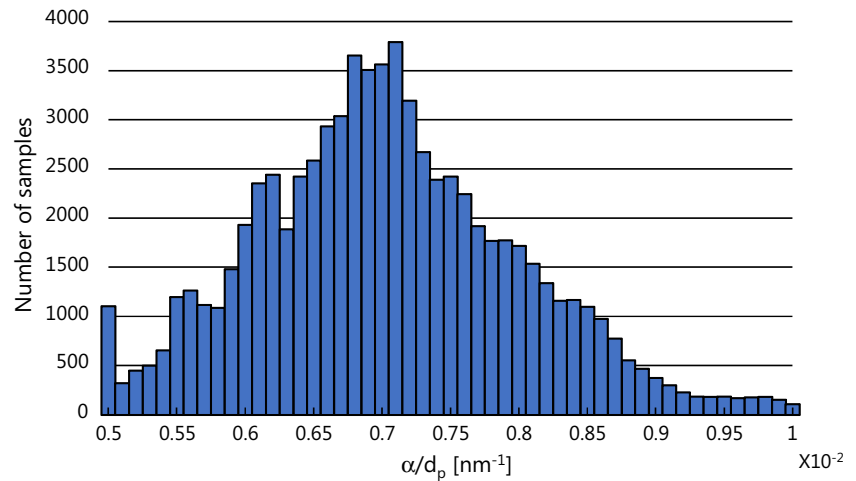
where $P(\mathbf{b}|\mathbf{x})$ is the likelihood of the observed data in \mathbf{b} occurring for a hypothetical \mathbf{x} , $P_{\text{pr}}(\mathbf{x})$ is a probability density that represents the state of knowledge of \mathbf{x} prior to the measurement, and $P(\mathbf{b})$ is the evidence

$$P(\mathbf{b}) = \int_{\mathbf{x}} P(\mathbf{b}|\mathbf{x})P_{\text{pr}}(\mathbf{x})d\mathbf{x} \quad (23)$$

which scales $P(\mathbf{x}|\mathbf{b})$ so that the Law of Total Probability is satisfied. In this study, the quantities-of-interest are the nanoparticle size and the TAC, $\mathbf{x} = [d_p, \alpha]^T$, while \mathbf{b} contains the expected values of the effective temperatures at various cooling times (i.e., the average of the effective temperatures obtained from individual shots, after outliers have been removed.) In contrast to Ref. [20], in which the effective temperatures in \mathbf{b} are assumed to be independent, considerable covariance was observed in \mathbf{b} , which likely arises from signal processing algorithms. We account for this by defining the variance-covariance matrix $\Gamma_{\mathbf{e}}$, again based on the effective temperatures obtained from individual shots, and then defining the likelihood as

$$P(\mathbf{b}|\mathbf{x}) \propto \exp \left\{ -\|(\mathbf{b}^{\text{mod}} - \mathbf{b}^{\text{exp}})\Gamma_{\mathbf{e}}^{-1}(\mathbf{b}^{\text{mod}} - \mathbf{b}^{\text{exp}})\|_2^2 \right\} \quad (24)$$

Fig. 12 Estimated posterior density for the Fe–CO data showing the density as a function of α/d_p during conduction only modeling. The regions of higher density correspond to values of α/d_p that are more likely



Uncertainties in the quantities-of-interest caused by uncertainties in the other “nuisance” model parameters, in this case $\Phi = [\rho, c_p, T_g, E(\mathbf{m})_r, P_g, T_{cr}, \Delta H_{v,b}]^T$, are incorporated into the analysis by treating them as additional stochastic variables to be inferred, so Bayes’ equation becomes

$$P(\mathbf{x}, \Phi | \mathbf{b}) = \frac{P(\mathbf{b} | \mathbf{x}, \Phi) P_{\text{pr}}(\mathbf{x}) P_{\text{pr}}(\Phi)}{P(\mathbf{b})} \quad (25)$$

While an uninformative prior is used for \mathbf{x} (i.e., $P_{\text{pr}}(\mathbf{x}) = 1$), the analysis must incorporate prior probabilities that reflect the state of knowledge of the other model parameters, similar to the procedure followed by Crosland et al. [59]. In this work, the parameters in Φ are assumed to be normally distributed about their nominal values with a standard distribution of 10 %, which reflects the epistemic uncertainty associated with these parameters; for example, the range of values for $E(\mathbf{m})_r$ corresponding to the various ellipsometry measurements on molten iron summarized in Table 2 are within ± 10 % of the Drude theory prediction.

Finally, the nuisance parameters are “marginalized out” of the posterior density by integration,

$$P(\mathbf{x} | \mathbf{b}) = \int_{\Phi} P(\mathbf{x}, \Phi | \mathbf{b}) d\Phi \quad (26)$$

Instead of carrying out the integrations in Eqs. (23) and (26) explicitly, however, the marginalized posterior distribution $P(\mathbf{x} | \mathbf{b})$ is estimated using a Markov chain Monte Carlo (MCMC) procedure [60]. Nuisance parameters, Φ , are sampled directly from their prior distributions so as to keep the samples centered about their expected values. Error bounds correspond to one standard deviation of 75,000 MCMC samples.

Figure 12 shows a histogram estimating the density of MCMC samples for the Fe–CO data when considering conduction only cooling. Regions with a higher number

of samples correspond to values of Fe–CO that are more likely. These values do not necessarily correspond to values where the posterior is maximum as there are multiple other dimensions that have been marginalized in producing this plot. The spread of the samples gives an indication of the uncertainty in the inferred parameter.

References

1. L.A. Melton, Soot diagnostics based on laser heating. *Appl. Opt.* **23**(13), 2201–2208 (1984)
2. S. Schraml, S. Will, A. Leipertz, Simultaneous measurement of soot mass concentration and primary particle size in the exhaust of a DI diesel engine by time-resolved laser-induced incandescence (TIRE-LII). *SAE Paper*, no. 01-0146 (1999)
3. B.F. Kock, T. Eckhardt, P. Roth, In-cylinder sizing of diesel particles by time-resolved laser-induced incandescence (TR-LII). *Proc. Combust. Inst.* **29**(2), 2775–2782 (2002)
4. D.R. Snelling, G.J. Smallwood, F. Liu, O.L. Gulder, W.D. Bachalo, A calibration-independent laser-induced incandescence technique for soot measurement by detecting absolute light intensity. *Appl. Opt.* **44**(31), 6773–6785 (2005)
5. R.L. Vander Wal, T.M. Ticich, J.R. West, Laser-induced incandescence applied to metal nanostructures. *Appl. Opt.* **38**(27), 5867–5879 (1999)
6. A.V. Filipov, M.W. Markus, P. Roth, In-situ characterization of ultrafine particles by laser-induced incandescence: sizing and particle structure determination. *J. Aerosol Sci.* **30**(1), 71–87 (1999)
7. R. Starke, B. Kock, P. Roth, Nano-particle sizing by laser-induced incandescence (LII) in a shock wave reactor. *Shock Waves* **12**(5), 260–351 (2003)
8. B.F. Kock, C. Kayan, J. Knipping, H.R. Orthner, P. Roth, Comparison of LII and TEM sizing during synthesis of iron particle chains. *Proc. Combust. Inst.* **30**(1), 1689–1697 (2005)
9. A. Eremin, E. Gurentsov, C. Schulz, Influence of the bath gas on the condensation of supersaturated iron atom vapour at room temperature. *J. Phys. D Appl. Phys.* **41**(5), 1–5 (2008)
10. A. Eremin, E. Gurentsov, E. Popova, K. Priemchenko, Size dependence of complex refractive index function of growing nanoparticles. *Appl. Phys. B* **104**(2), 289–295 (2011)
11. A. Eremin, E. Gurentsov, E. Mikheyeva, K. Priemchenko, Experimental study of carbon and iron nanoparticle vaporisation under pulse laser heating. *Appl. Phys. B* **112**(3), 421–432 (2013)

12. Y. Murakami, T. Sugatani, Y. Nosaka, Laser-induced incandescence study on the metal aerosol particles as the effect of the surrounding gas medium. *J. Phys. Chem. A* **109**(40), 8994–9000 (2005)
13. T. Sipkens, G. Joshi, K.J. Daun, Y. Murakami, Sizing of molybdenum nanoparticles using time-resolved laser-induced incandescence. *J. Heat Transf.* **135**(5), 052401 (2013)
14. J. Reimann, H. Oltmann, S. Will, C. Bassano, E.L. Lösch, S. Günther, Laser Sintering of Nickel Aggregates Produced from Inert Gas Condensation. in *Proceedings of the World Conference on Particle Technology*, Nuremberg, Germany (2010)
15. T. Lehre, H. Bockhorn, B. Jungfleisch, R. Suintz, Development of a measuring technique for simultaneous in situ detection of nanoscaled particle size distributions and gas temperatures. *Chemosphere* **51**, 1055–1061 (2003)
16. S. Maffi, F. Cignoli, C. Bellomunno, S. De luliis, G. Zizak, Spectral effects in laser induced incandescence application to flame-made titania nanoparticles. *Spectrochim. Acta B* **63**(2), 202–209 (2009)
17. F. Cignoli, C. Bellomunno, S. Maffi, G. Zizak, Laser-induced incandescence of titania nanoparticles synthesized in a flame. *Appl. Phys. B* **96**(4), 593–599 (2008)
18. B. Tribalet, A. Faccinetto, T. Dreier, C. Schultz, Evaluation of particle sizes of iron-oxide nano-particles in a low-pressure flame-synthesis reactor by simultaneous application of TiRe-LII and PMS. in *5th Workshop on Laser-Induced Incandescence*, Le Touquet, France (2012)
19. I.S. Altman, D. Lee, J.D. Chung, J. Song, M. Choi, Light of absorption of silica nanoparticles. *Phys. Rev. B* **63**(16), 161402 (2001)
20. T.A. Sipkens, R. Mansmann, K.J. Daun, N. Petermann, J.T. Titantah, M. Karttunen, H. Wiggers, T. Dreier, C. Schulz, In situ particle sizing of silicon nanoparticles by time-resolved laser-induced incandescence. *Appl. Phys. B* **116**(3), 623–636 (2014)
21. S. Krishnan, K.J. Yugawa, P.C. Nordine, Optical properties of liquid nickel and iron. *Phys. Rev. B* **55**(13), 8201–8206 (1997)
22. J.C. Miller, Optical properties of liquid metals at high temperatures. *Philos. Mag.* **20**(168), 1115–1132 (1969)
23. K.M. Shvarev, V.S. Gushchin, B. Baum, The effect of temperature on optical constants of iron. *High Temp.* **16**(3), 441–446 (1978)
24. K.K. Nanda, F.E. Kruijs, H. Fissan, Evaporation of free PbS nanoparticles: evidence of the Kelvin effect. *Phys. Rev. Lett.* **89**(25), 256103 (2002)
25. K. Daun, B. Stagg, F. Liu, G. Smallwood, D. Snelling, Determining aerosol particle size distributions using time-resolved laser-induced incandescence. *Appl. Phys. B* **87**(2), 363–372 (2007)
26. T.C. Bond, R.W. Bergstrom, Light absorption by carbonaceous particles: an investigative review. *Aerosol Sci. Technol.* **40**, 27–67 (2006)
27. M.F. Modest, *Radiative Heat Transfer*, 3rd edn. (Academic Press, San Diego, 2013)
28. J.A. Creighton, D.G. Eadon, Ultraviolet–Visible absorption spectra of the colloidal metallic elements. *J. Chem. Soc., Faraday Trans.* **87**, 3881–3891 (1991)
29. M. Quinten, *Optical Properties of Nanoparticle Systems: Mie and Beyond* (Wiley, New York, 2011)
30. C.F. Bohren, D.R. Huffman, *Absorption and Scattering of Light by Small Particles* (Wiley, New York, 1983)
31. M.P. Marder, *Condensed Matter Physics*, 2nd edn. (Wiley, New York, 2010)
32. Y. Liu, S.A. Majetich, R.D. Tilton, D.S. Scholl, G.V. Lowry, TCE dechlorination rates, pathways, and efficiency of nanoscale iron particles with different properties. *Environ. Sci. Technol.* **39**(5), 1338–1345 (2005)
33. F. He, D. Zhao, Manipulating the size and dispersibility of zero-valent iron nanoparticles by use of carboxyl cellulose stabilizers. *Environ. Sci. Technol.* **41**(17), 6216–6221 (2007)
34. M. W. Chase, *NIST-JANAF Thermochemical Tables*, 4th edn. American Institute of Physics (1998)
35. H. Kobatake, H. Khosroabadi, H. Fukuyama, Normal spectral emissivity measurement of liquid iron and nickel using electromagnetic levitation in direct current magnetic field. *Metall. Mater. Trans. A* **43A**, 2466–2472 (2012)
36. K.J. Daun, T.A. Sipkens, J.T. Titantah, M. Karttunen, Thermal accommodation coefficients for laser-induced incandescence sizing of metal nanoparticles in monatomic gases. *Appl. Phys. B* **112**(3), 409–420 (2013)
37. F. Liu, K.J. Daun, D.R. Snelling, G.J. Smallwood, Heat conduction from a spherical nanoparticle: status of modeling heat conduction in laser-induced incandescence. *Appl. Phys. B* **83**, 355–382 (2006)
38. K.J. Daun, Thermal accommodation coefficients between polyatomic gas molecules and soot in laser-induced incandescence experiments. *Int. J. Heat Mass Transf.* **52**, 5081–5089 (2009)
39. K.J. Daun, G.J. Smallwood, F. Liu, Investigation of thermal accommodation coefficients in time-resolved laser-induced incandescence. *J. Heat Transf.* **130**(12), 121201 (2008)
40. K.J. Daun, G.J. Smallwood, F. Liu, Molecular dynamics simulations of translational thermal accommodation coefficients for time-resolved LII. *Appl. Phys. B* **94**(1), 39–49 (2009)
41. K.J. Daun, J.T. Titantah, M. Karttunen, Molecular dynamics simulation of thermal accommodation coefficients for laser-induced incandescence sizing of nickel particles. *Appl. Phys. B* **107**(1), 221–228 (2012)
42. K.M. Watson, Thermodynamics of the liquid state. *Ind. Eng. Chem.* **35**(4), 398–406 (1943)
43. D.A. Young, B.J. Alder, Critical point of metals from the van der Waals model. *Phys. Rev. A* **3**(1), 364–371 (1971)
44. D. Lide (ed.), *CRC Handbook of Chemistry and Physics*, 95th ed., (CRC Press, Boca Raton, 2014–2015)
45. W. Forsythe, *Smithsonian Physical Tables*, 9th ed., Knovel (2003)
46. P.D. Desai, Thermodynamic properties of iron and silicon. *J. Phys. Chem. Ref. Data* **15**(3), 967–983 (1986)
47. S.A. Kuhlmann, J. Reimann, S. Will, On heat conduction between laser-heated nanoparticles and a surrounding gas. *J. Aerosol Sci.* **37**(12), 1696–1716 (2006)
48. B.J. Keene, Review of data for the surface tension of iron and its binary alloys. *Int. Mater. Rev.* **33**(1), 1–37 (1988)
49. R.C. Tolman, The effect of droplet size on surface tension. *J. Chem. Phys.* **17**(3), 333–337 (1949)
50. K. Koga, X.C. Zeng, A.K. Shchekin, Validity of Tolman’s equation: how large should a droplet be? *J. Chem. Phys.* **109**(10), 4063–4070 (1998)
51. T. Mohri, T. Horiuchi, H. Uzawa, M. Ibaragi, M. Igarashi, F. Abe, Theoretical investigation of L10-disorder phase equilibria in Fe–Pd alloy system. *J. Alloys Compd.* **317**, 13–18 (2001)
52. Y.A. Lei, T. Bykov, S. Yoo, X.C. Zeng, The Tolman length: is it positive or negative? *J. Am. Chem. Soc.* **127**(44), 15346–15347 (2005)
53. H.M. Lu, Q. Jiang, Size-dependent surface tension and Tolman’s length of droplets. *Langmuir* **21**(2), 779–781 (2005)
54. A.R. Nair, S.P. Sathian, Studies on the effect of curvature on the surface properties of nanodrops. *J. Mol. Liq.* **195**, 248–254 (2014)
55. J.H. Shin, M.R. Deinert, A model for the latent heat of melting in free standing metal nanoparticles. *J. Chem. Phys.* **140**(16), 164707 (2014)
56. A. Alqudami, S. Annapoorni, Fluorescence from metallic silver and iron nanoparticles prepared by exploding wire technique. *Plasmonics* **2**, 5–13 (2007)

57. R.L. Vander Wal, Laser-induced incandescence: excitation and detection conditions, material transformations and calibration. *Appl. Phys. B* **96**(4), 601–611 (2009)
58. T. Phenrat, H.J. Kim, F. Fagerlund, T. Illangasekare, R.D. Tilton, G.V. Lowry, Particle size distribution, concentration, and magnetic attraction affect transport of polymer-modified FeO nanoparticles in sand columns. *Environ. Sci. Technol.* **43**(15), 5079–5085 (2009)
59. B.M. Crosland, M.R. Johnson, K.A. Thomson, Analysis of uncertainties in instantaneous soot volume fraction measurements using two-dimensional, auto-compensating, laser-induced incandescence (2D-AC-LII). *Appl. Phys. B* **102**, 173–183 (2011)
60. J. Kaipio, E. Somersalo, *Statistical and Computational Inverse Problems* (Springer, Berlin, 2005)